

A compact, fast, wide-field imaging spectrometer system

Pantazis Mouroulis^{*a}, Byron E. Van Gorp^a, Victor E. White^a, Jason M. Mumolo^a, Daniel Hebert^b,
Martin Feldman^b

^aJet Propulsion Laboratory, California Institute of Technology, Pasadena, CA USA 91109;

^bDept. of Elec. & Computer Eng., Louisiana State University, Baton Rouge, LA USA 70803-5901

ABSTRACT

We present test results from a compact, fast (F/1.4) imaging spectrometer system with a 33° field of view, operating in the 450-1650 nm wavelength region with an extended response InGaAs detector array. The system incorporates a simple two-mirror telescope and a steeply concave bilinear groove diffraction grating made with gray scale x-ray lithography techniques. High degree of spectral and spatial uniformity (97%) is achieved.

Keywords: imaging spectrometry, Dyson spectrometer, diffraction grating, x-ray lithography

1. INTRODUCTION

Reflectance spectroscopy of dark or dimly lit targets such as water or remote solar system bodies requires a high-throughput spectrometer. The Dyson spectrometer¹⁻³ has been shown to be capable of providing high throughput while at the same time permitting a compact size and high uniformity of response⁴. In this paper, we demonstrate a compact, fast, uniform imaging spectrometer operating in the visible and short wave infrared region. The Dyson design has already flown in space⁵ although the instrument operated at an effective aperture of F/3 and thus did not specifically exploit the high throughput potential of the design form. More recently, thermal infrared spectrometers based on the Dyson form have been developed^{6,7} but a design at those longer wavelengths can take advantage of the high refractive index of available materials (e.g., ZnSe) in order to achieve high numerical aperture. In the visible and short-wave infrared regime, the materials of choice will be fused silica or CaF₂ which have a much lower refractive index. The system design pursued here is fundamentally similar to the one proposed by Mouroulis et al⁸ for a coastal ocean spectrometer, but it further extends the wavelength range from that of a Si-based detector to that of an extended-response InGaAs detector, and further increases the throughput (F/1.4 vs. F/1.8).

Crucial to the spectrometer design is a diffraction grating that can be formed on a steeply concave substrate and that will have an optimized wavelength response over the entire range. X-ray fabrication techniques^{9,10} are well suited to this task. We present here a novel, extended response grating with a sag of 4 mm that enables this spectrometer design.

A high-throughput system must strive to minimize the number of optical surfaces. To that end, the other innovation employed in this system is an inexpensive F/1.4 two-mirror telescope with a snap-and-bond assembly and alignment method. The complete system has been tested for spectral and spatial response as well as uniformity. The term uniformity here implies the degree of orthogonality between spectral and spatial information, which is primarily the lack of geometric distortion, as well as the uniformity of the spectral response through field and of the spatial response through wavelength.⁴ The system specifications are shown in Table 1.

2. OPTICAL DESIGN

The telescope comprises two conics with a common axis of symmetry, of which off-axis portions are used. A raytrace is shown in Fig. 1. Even though a slight mirror decenter or tilt can potentially improve the optical performance by a small amount, the advantage of maintaining the axis of symmetry is significant in implementing a simple alignment method. As can be seen from Fig. 1, the telescope does not possess a real pupil. For a telecentric output beam (matching the Dyson spectrometer to follow) the stop is located a short distance behind the primary mirror. The two mirrors are oversized sufficiently to avoid vignetting and allow the spectrometer to set the system aperture.

*pantazis.mouroulis@jpl.nasa.gov; phone 1 818 393-2599; fax 1 818 393 6869

The Dyson spectrometer utilizes a fused silica lens and incorporates a built-in fold mirror to allow the detector sufficient clearance from the slit. The raytrace is shown in Fig. 2. The distance between slit and grating is ~12 cm. Both powered surfaces (lens and grating) are spherical.

Table 1. First order system specifications.

Parameter	Value
Spectral band	400-1650 nm
Spectral sampling	4.95 nm
Swath width	33°
Spatial pixels	640
Pixel size	25 μm
F-number	1.4
Slit width	27 μm
Operating T (detector)	285 K

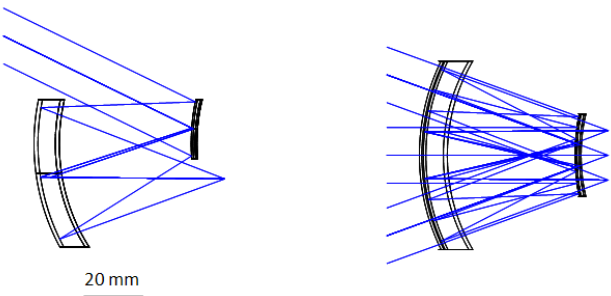


Figure 1. Telescope raytrace in two planes. The telecentric output beam for three field points is shown on the right.

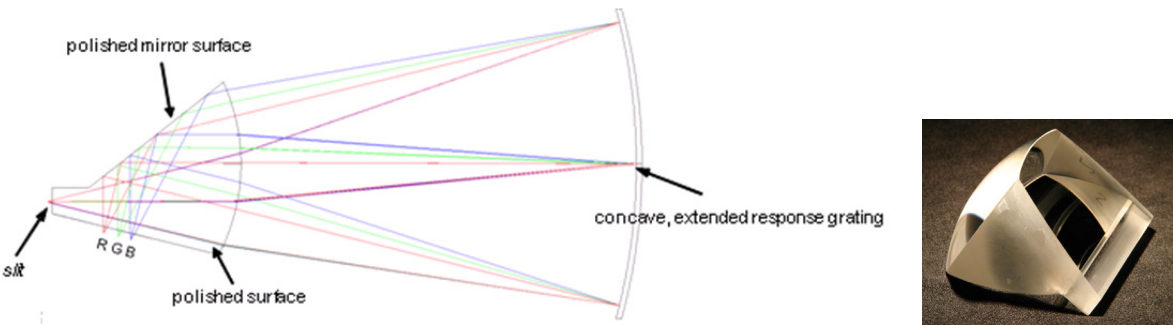


Figure 2. Spectrometer raytrace and photograph of monolithic fused silica block (manufactured by Optimax).

The optical performance of the design can be summarized as follows. The energy in a 25 μm square is >95% for the telescope at all fields. The y-enslitted energy within a 25 μm slit (characteristic of spectral response uniformity) is >90% for the spectrometer for all wavelengths. The same holds for the x-enslitted energy, which characterizes the spatial response uniformity with wavelength.

3. OPTO-MECHANICAL DESIGN AND ASSEMBLY

The opto-mechanical design takes full advantage of the axisymmetric property of both the telescope and spectrometer subassemblies. The design is shown in Fig. 3.

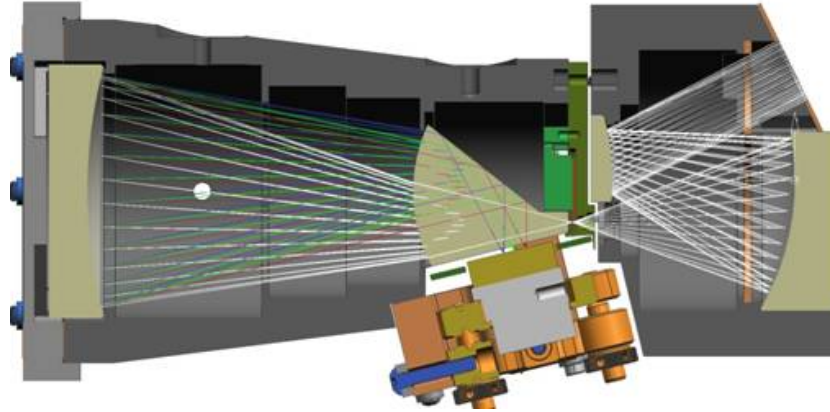


Figure 3. Optomechanical bench assembly. A baffle tube is omitted from the input side.

Starting with the telescope, the two mirrors are made on glass substrates and are bonded to the aluminum housing, with mismatch in thermal expansion being of no concern for this room-temperature system. The mirrors are aligned by being seated against precisely machined edges, similar to the alignment tubes used for rotationally symmetric lens assemblies. The substrates are oversized to ensure secure seating of the mirrors. The conic constants of the surfaces are small enough to allow this simple assembly. Each mirror in turn is placed against its seat and adhesive is injected in the gap. Discounting adhesive setting time, the operation can be completed within approximately 1 hr. Following assembly, the wavefront error of the telescope was measured interferometrically. The result is shown in Fig. 4, and is compared with the design error. Small deviations from the axisymmetric condition can actually improve the performance of this telescope, and this is what is observed in Fig. 4. In any case, it may be seen that this very simple assembly method succeeded in meeting the wavefront specification of the telescope.

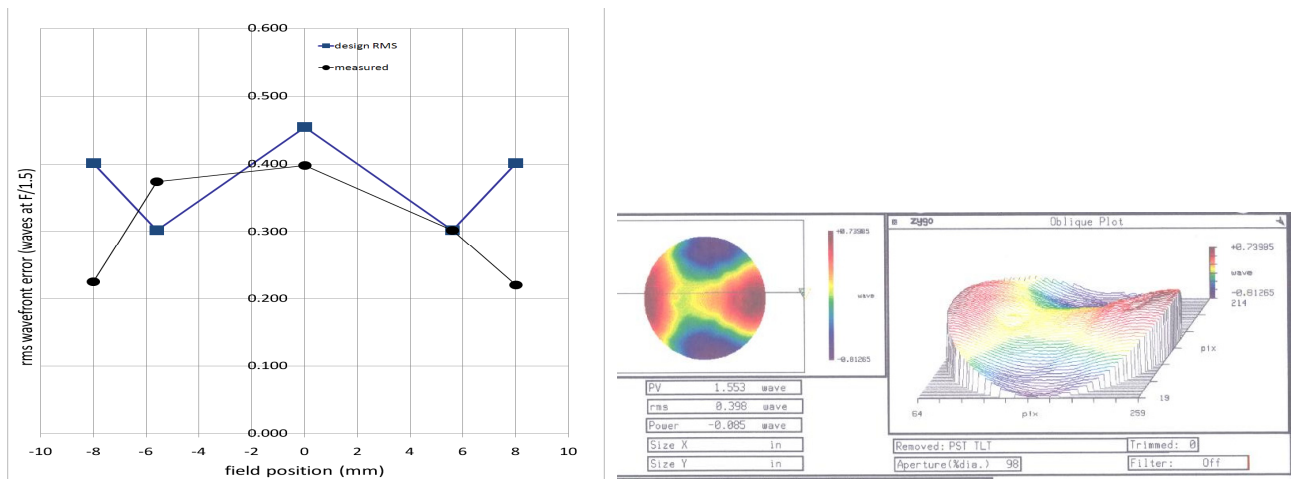


Figure 4. RMS wavefront error of the telescope through field. Squares: design, circles: measurement. The field position in mm corresponds to the length of the slit. An interferogram near the middle of the field is also shown.

The two optical elements of the spectrometer are aligned in a similar fashion, by simply pushing against precisely machined edges. In this case, the grating is bonded to a tight-fitting aluminum ring that is allowed to rotate by a small

amount, $\sim \pm 1^\circ$ through a flexure in order to achieve the required rotational alignment of fractions of mrad relative to the slit. The grating remains well centered through this motion. The expected and measured wavefront error near the middle of the field are shown in Fig. 5.

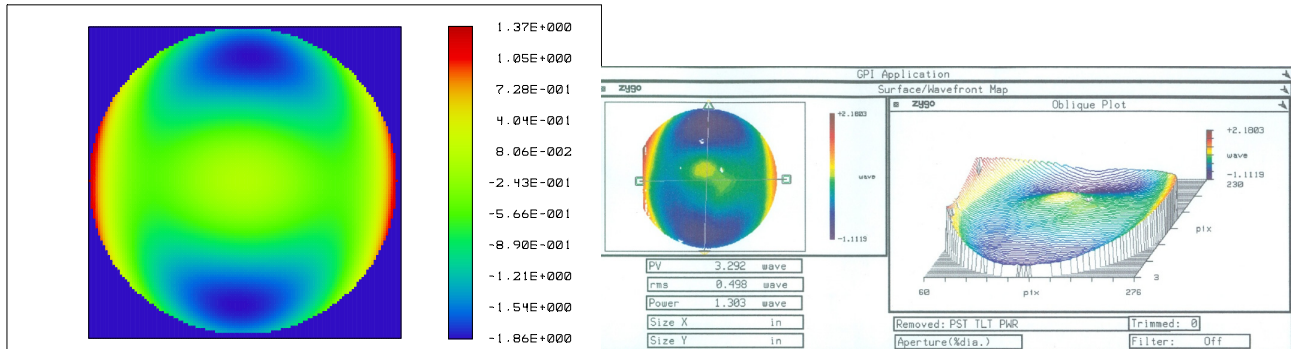


Figure 5. RMS Expected and measured spectrometer wavefront error near the middle of the field. Close agreement is seen in the type and amount of error. The small amount of vignetting seen on the left side of the interferogram is due to a portion of the grating that was shaded during the recording process.

Cost considerations led to the choice of a commercial mount for the detector array, which provides tip, tilt, and translation (focus), but no rotation (clocking relative to slit). This required degree of freedom was implemented by having the slit itself placed on a mount that permits a small amount of rotation. The telescope is attached to the spectrometer body through precision pins and bolts. A shim may be inserted to adjust the focus if necessary. The completed optomechanical assembly except for the detector array is shown in Fig. 6.

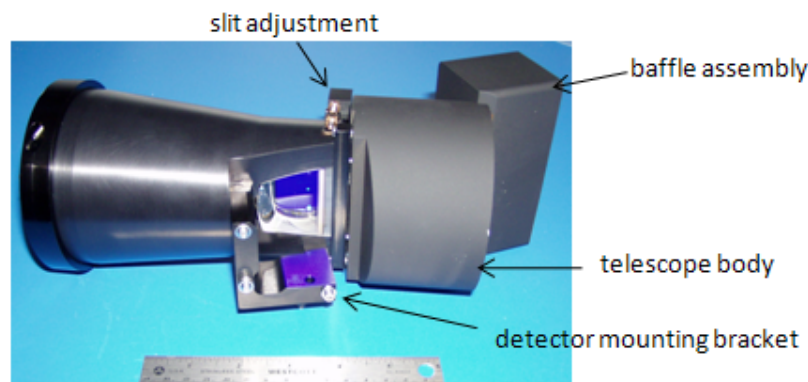


Figure 6. Complete optomechanical assembly showing telescope attached to the spectrometer body and entrance baffle assembly. The ruler is 152 mm long.

4. X-RAY LITHOGRAPHY DIFFRACTION GRATING

The requirement for a broad band concave diffraction grating with a sag of approximately 4 mm makes gray-scale X-ray lithography^{9,10} the preferred technique. Among competing techniques the best candidate is electron-beam lithography because of the high-quality gratings it has been shown to produce¹¹. However, the required sag was beyond the capability of the e-beam technique at the time of initiating this effort. X-ray lithography permits the use of any substrate, which is coated with an appropriate resist (in this case, PMGI resist from Microchem Corporation). The resist is then exposed through an X-ray mask while the substrate is translated linearly behind the mask. The shape of the mask determines the exposure, and can be made to correct for the inherent nonlinearity of the process. A portion of the mask and a finished grating are shown in Fig. 7. Each opening is made of two segments with different mean slope, and each

segment is curved to account for nonlinearity. Five rows of openings were used in total. By increasing the number of rows, the exposure time can be decreased, which is significant for a large grating (67mm diameter or length of scan). However, this increases the probability of periodic mask errors that can generate ghosts.

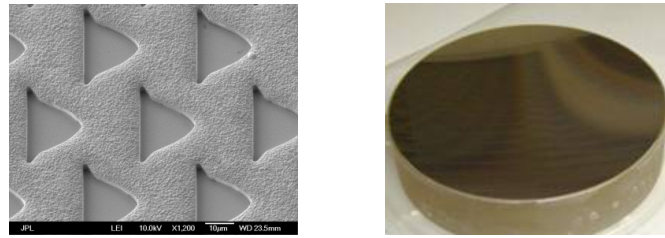


Figure 7. Left: Scanning electron microscope image of the X-ray mask. The horizontal length of the feature (grating period) is approximately 20 μm . Right: A finished grating on a fused silica substrate.

As is evident from Fig. 5, the grating does not contribute any significant wavefront irregularity to the overall system wavefront error, thus demonstrating a sufficiently uniform resist coating. The intended groove shape was bilinear, so that each groove would comprise two different segments with different slopes. This serves to broaden the grating response. A profilometer scan of the groove of a flat witness sample exposed and developed together with the concave grating is shown in Fig. 8. The groove comprises a steeper short segment (between about 18 and 20 μm) and a larger segment with more moderate slope (between 4 and 18 μm), corresponding to the two parts of the mask seen in Fig. 7. The slope of the leftmost segment is ideally close to infinite, however there is significant rounding from the profilometer stylus.

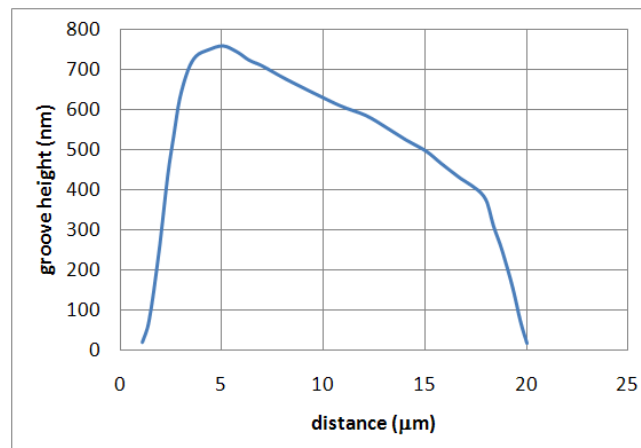


Figure 8. Approximately bilinear groove profile taken with a stylus profilometer from a flat witness sample.

The measured efficiency of this grating is shown in Fig. 9. The curve has a FWHM of about 1230 nm, which is significantly broader than what a typical sawtooth profile would give (~870 nm). Of course at the same time the peak efficiency is lower. The efficiency was measured by illuminating the entire grating aperture at once by placing a large numerical aperture multimode fiber near the center of curvature of the grating and collecting the light in the first order. Care was taken to ensure uniform illumination of the entire aperture by exciting all fiber modes. The resulting efficiency curve is smoother than would be expected from an ideal bilinear profile. This is due to mask imperfections which generate slightly different grooves along the extent of the grating, each with a slightly different efficiency. However, the net result is very close to the desired efficiency both in terms of peak value and width of the band. The band matches exactly that of the InGaAs detector response.

The same setup used for efficiency measurement can also be used to characterize the stray light characteristics. In this case, a slit is scanned between the zero and first orders (and beyond). The results may be summarized by stating that the scatter floor in the spectral direction reaches $1\text{E-}4$, but there is a spectral ghost at the level of $\sim 3\text{E-}4$ corresponding to a frequency of twice the fundamental. This is considered satisfactory as judged against a requirement of $< 1\text{E-}3$. Previous gratings that were made with the same technique but used only a single row mask did not exhibit this ghost and we surmise it arises from periodic errors in the multiple-row mask. In the spatial direction, all these gratings exhibit a weak ($< 1\text{E-}4$) spatial ghost that is due to the stepper motor of the scanning stage. Overall, this grating met all the goals for wavefront quality, efficiency, and stray light.

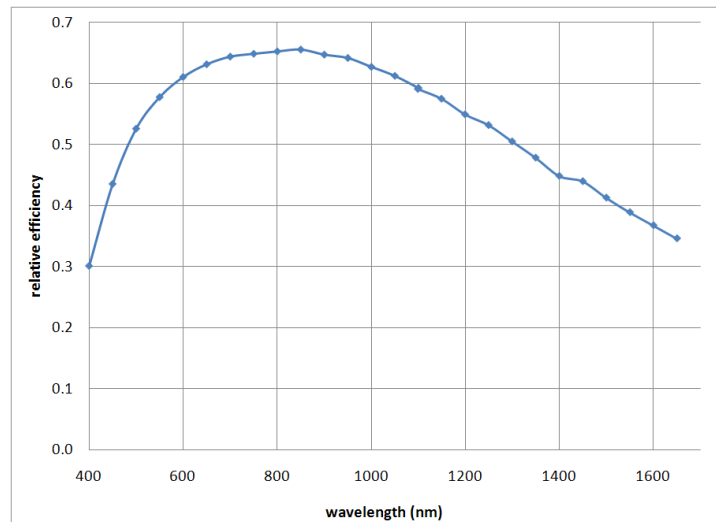


Figure 9. Measured efficiency of bilinear groove grating.

5. EXTENDED RESPONSE InGaAs PHOTODETECTOR ARRAY

A custom-packaged commercial InGaAs array was procured for this work (Fig. 10). The array has a 640×512 format with $25\text{ }\mu\text{m}$ square pixels. The package allows for the tight clearance between the fused silica block and the surface of the detector as well as the proximity to the slit assembly. As the system was not sealed or purged, the detector was operated at around 285K , which is higher than its recommended temperature of $\sim 250\text{K}$. This would have an effect at least on dark current performance; however the system characteristics that we sought to prove were not dark-current limited.

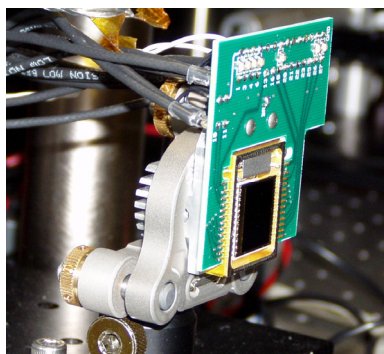


Figure 10. Custom-packaged InGaAs array shown in its adjustment mount, during linearity and reflectivity tests.

The photodetector material is thinned so as to extend the response to the visible part of the spectrum. The quantum efficiency of the array can be gauged to a certain extent by its reflectivity which is shown in Fig. 11. The sharp peak at

450 nm is undesirable and can be a cause of stray light in a Dyson spectrometer. A more sophisticated anti-reflection coating will be required for demanding imaging spectrometry applications.

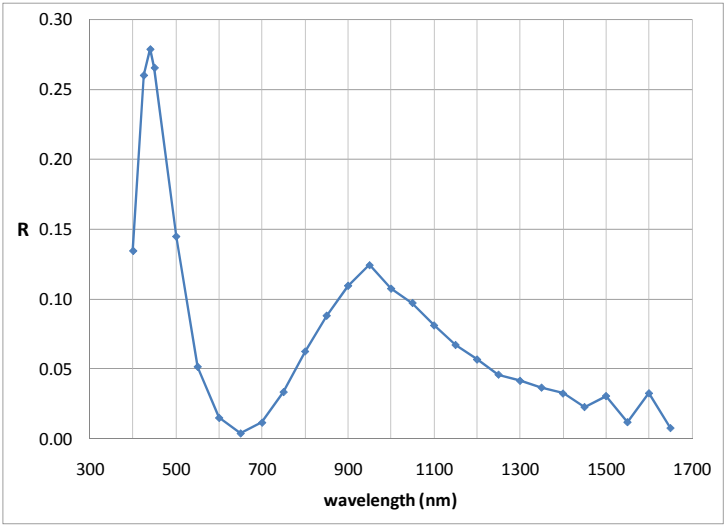


Figure 11. InGaAs array reflectivity through wavelength.

Of even greater significance is the linearity characteristic and the substantial variation in response observed across the array. The linearity was measured by using a NIST-traceable integrating sphere source placed at a known distance (~1m) from the array without any intervening optics. The source intensity can change without affecting the spectral content of the radiation. As can be seen in Fig. 12, strong nonlinearity was observed, with substantial variation across the array. A correction was implemented on a pixel basis through spline fitting. Nevertheless, with the required correction being so large and variable small imperfections will inevitably remain in the processed data.

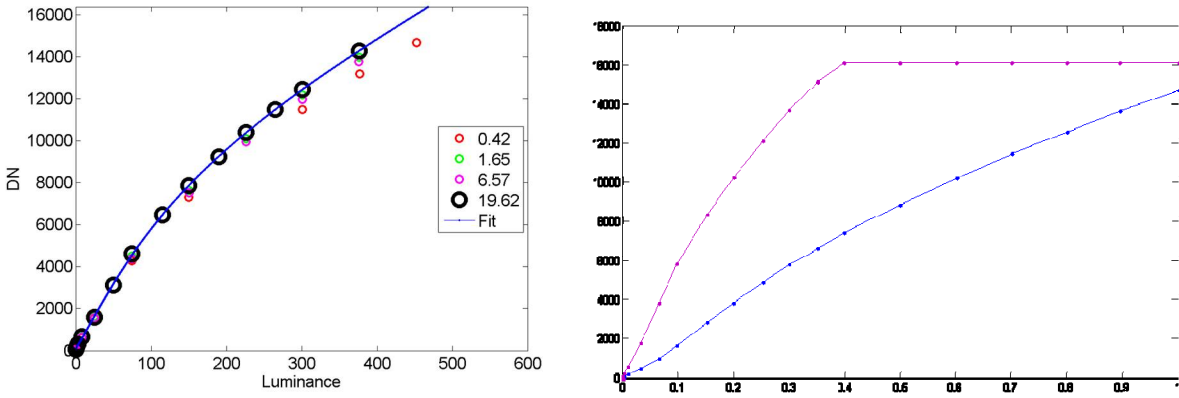


Figure 12. Left: Linearity characteristics of a single sample pixel at various integration times in s, shown in the inset. Right: Variation of linearity and gain characteristics across the array, showing the two extreme cases of highest and lowest gain.

6. SYSTEM CHARACTERIZATION

For testing, the spectrometer assembly was mounted on a large goniometric stage that could rotate by more than the telescope field of view. The rotation was about the center of the telescope entrance pupil, so that a fixed collimated beam, in conjunction with the stage rotation could be used to illuminate any part of the field. Appropriate compensation for beam walk was implemented through a motorized fold mirror. This beam walk is due to the curvature of the slit

image as projected by the telescope, which in turn is a consequence of the distortion inherent in a wide field system. This distortion is not generally a cause of image or spectral artifacts and is routinely corrected through image post-processing.

At the focal plane of the collimator are placed three targets: 1) a ground glass diffuser illuminated by a monochromator that can be scanned in wavelength to derive the spectral response function (SRF), 2) a vertically scanned slit, illuminated with white light, that is used to derive the cross-track spatial response function (CRF) at all wavelengths, and 3) a horizontally-scanned slit that is used to derive the along-track spatial response function (ARF). In addition, a removable integrating sphere illuminated with lasers is placed directly in front of the telescope to illuminate the entire field and derive the spectral uniformity characteristics. This testing method is used both for calibration and alignment of the focal plane array, telescope, and grating.

6.1 Geometric uniformity

There are two geometric distortion errors that affect the uniformity of response: 1) the variation of the CRF centroid location with wavelength (also known as “keystone”), and 2) the variation of the SRF centroid with field (also known as “smile”). These were assessed by calculating the centroids of a white-light point source and of an extended laser source respectively. Details of the method have been provided in ref. 12.

Figure 13 shows the summary result of keystone characterization. Centroids are obtained at five field points spanning the cross-track field. A linear fit is obtained for each of five series. The mean of the five slopes represents imperfect grating clocking and is correctable by more precise adjustment. In order to obtain a single number characterizing the entire spectrometer non-uniformity, the maximum differences are obtained between the data at any one pixel from all five series and are then plotted as a separate series. From this series the mean slope is subtracted; the result represents the inherent spectrometer keystone that cannot be improved by any further adjustments. As Fig. 13 shows, the inherent error is less than 2% of a pixel over the specific data range.

The centroiding procedure fails where the signal is rapidly diminishing at both ends of the spectrum due to increased noise. The signal drop is due to a blue-poor source spectrum at the short end and to a rapid decrease in detector quantum efficiency at the long end. In order to extrapolate to the full spectral range, the interpolated quadratic curve of Fig. 13 can be used. The data of Fig. 13 span the range 621-1611 nm. Extrapolation to the range 400-1650 nm yields a value of just around 2%. Higher order polynomial provides only small improvement in the fit and is not physically justifiable.

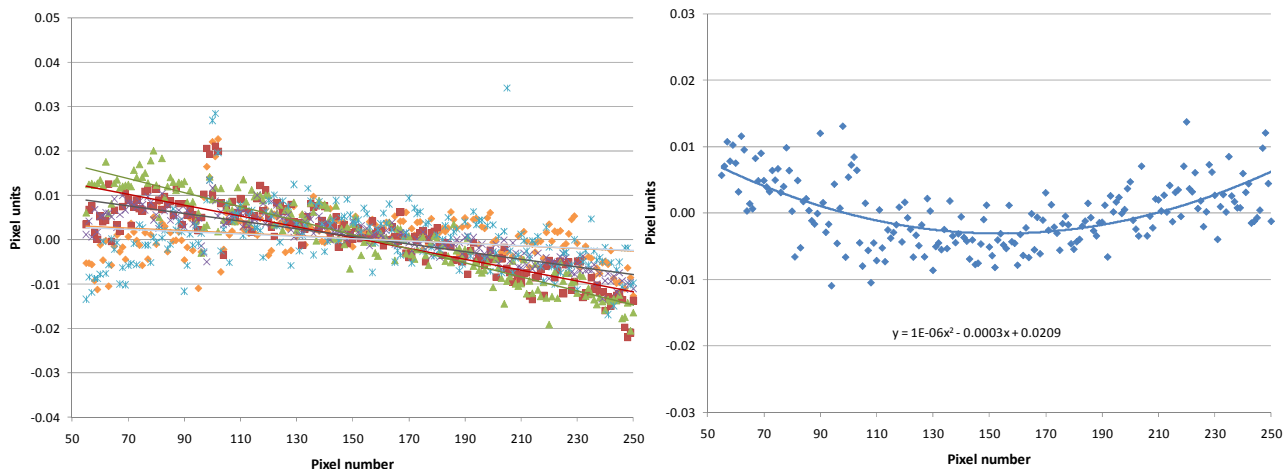


Figure 13. Left: Centroid data for five field points. The horizontal axis represents spectral channel number. Right: maximum difference between all data points of left chart with mean slope subtracted represents the inherent keystone effect of the spectrometer.

The spectral uniformity (or smile) is assessed in Fig. 14, where we used two laser wavelengths near the opposite ends of the spectrum (532 nm and 1340 nm, the second one being actually 670 nm observed in second order, made possible by the lack of order-sorting filter). The centroids along the length of the entire slit show a similar 4th order polynomial shape but a small slope difference. In plotting these, a mean slope of approximately 1% of a pixel has been subtracted, representing a slight clocking error of the slit that is correctable with more precise alignment.

Neither the net slope difference nor the high-order residuals are physically justified and for this reason we believe the residual smile to be mostly due to measurement inaccuracy caused primarily by the difficulty of performing a large pixel-by-pixel gain and linearity correction. In any case, even taken at face value the data of Fig. 14 show a net smile of just less than 3% of a pixel.

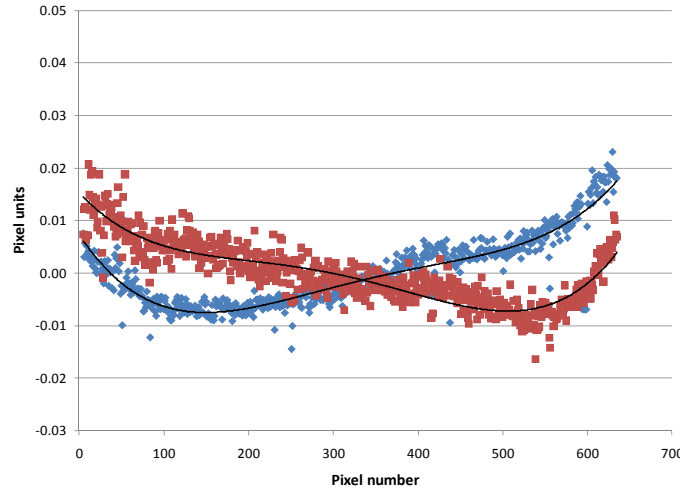


Figure 14. Centroid data for two laser wavelengths spanning the full field of 640 pixels. The extreme values of each curve represent the net smile inherent in the spectrometer.

6.2 Spectral response function

The spectral response function was assessed with a scanning monochromator, as noted in the introduction to this section, across the entire wavelength range and for five field points spanning the instrument FOV. An example set of SRFs around the 625 nm wavelength and for the middle of the field is shown in Fig. 15. The curves shown represent the raw data, not Gaussian interpolation. All other curves through field and wavelength have very similar shapes and widths. Table 2 shows the variation through field of the SRF full width at half-maximum for three representative wavelengths.

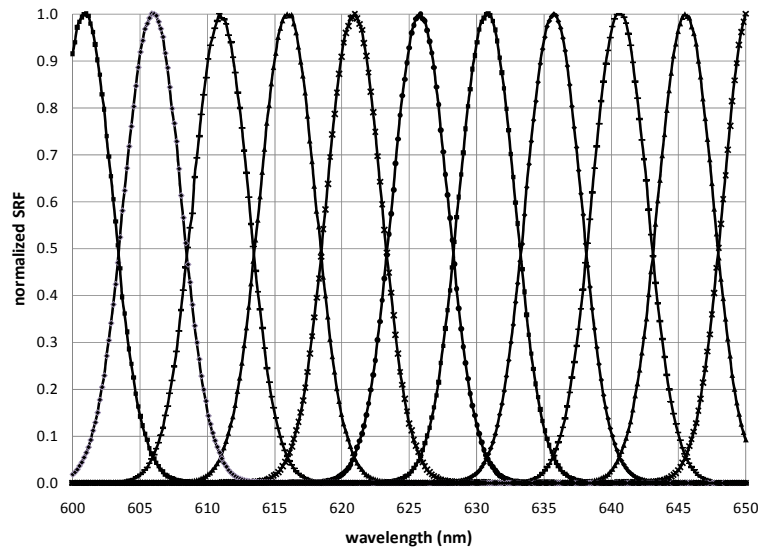


Figure 15. Measured spectral response functions of spectral channels around 625 nm for the middle of the field.

The table shows the response variation through field for each wavelength in percentage, normalized to one end of the field. The maximum variation for any wavelength is <5%. It is known that the effect on spectral calibration of the SRF FWHM non-uniformity is approximately half that of the SRF centroid¹³ on the same percentage basis, hence a maximum FWHM error of 4.6% is approximately the same as a centroid error of 2.3%.

Table 2. Spectral response function FWHM variation through field for three wavelengths

Field angle	625 nm	1125 nm	1625 nm
-15	1.7%	-1.3%	-0.9%
-8	-1.3%	-1.6%	-3.0%
0	-2.6%	-3.4%	-4.6%
8	-2.0%	-2.1%	-3.1%
15	0.0%	0.0%	0.0%

6.3 Cross-track spatial response function

The CRF is assessed through a sub-pixel slit scanned in the perpendicular direction to the instrument slit. White light illumination with spectral balance filters allows simultaneous assessment of all spectral channels. A check was made, using a long-pass filter, to confirm that the lack of order-sorting filter over the detector (and consequent mixing of orders) did not affect the CRF width or shape in any measurable way. Typical CRF curves are shown in Fig. 16 for seven adjacent spatial channels. These show some noise, traced to a detector timing issue, and also a weak ghost on the left side, caused by the detector readout. These issues would need to be addressed in an eventual flight system, but are not fundamental and can also be corrected with a Gaussian fit.

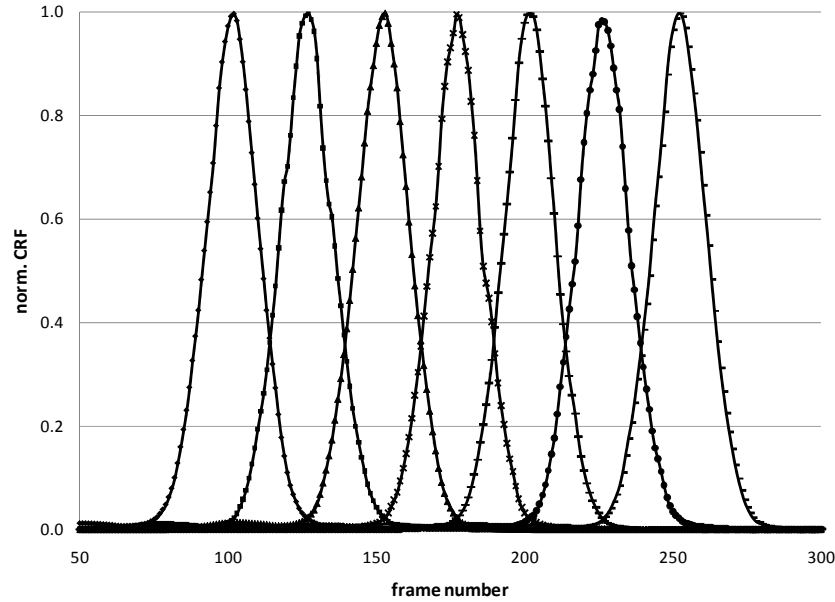


Figure 16. Measured cross-track spatial response functions of spatial pixels near the -15° field point and for the 1220 nm wavelength.

The CRF centroid uniformity has been shown in Sec. 6.1. There remains the variation of the CRF width with wavelength. Table 3 shows the variation at different fields. Like the SRF, the CRF FWHM variation also equivalent to approximately half the centroid variation, so the non-uniformity effect of Table 3 is comparable to that of Fig. 13.

Table 3. Cross-track spatial response function FWHM variation through wavelength for three fields

wavelength	15 deg	0 deg	-15 deg
620	0.0%	0.0%	0.0%
960	1.8%	1.0%	0.1%
1270	4.3%	0.5%	2.2%
1600	6.6%	-1.3%	5.7%

6.4 Along-track spatial response function

The ARF is assessed through a sub-pixel slit scanned parallel to the instrument slit. White light illumination allows simultaneous assessment of all spectral channels. In terms of uniformity, the important question is the variation of the response with wavelength, rather than field. The ARF is shown in Fig. 17 for the middle of the field and four different wavelengths. Except for some noise near the top, the curves are almost indistinguishable, indicating excellent wavelength uniformity. The uniformity through wavelength is similar at other field points, and is basically due to the high numerical aperture of the telescope leading to small diffraction spot relative to the slit even for the longest wavelength. The ARF in Fig. 17 is designated as “static” because it lacks the motion smear that would result from an operational sensor. Such smear would tend to make the response more Gaussian or triangular in shape. It can be simulated by further convolving this result with a rect or similar function corresponding to the integration time and flight speed, if desired. In any case, this result shows that the telescope meets its design resolution at system level.

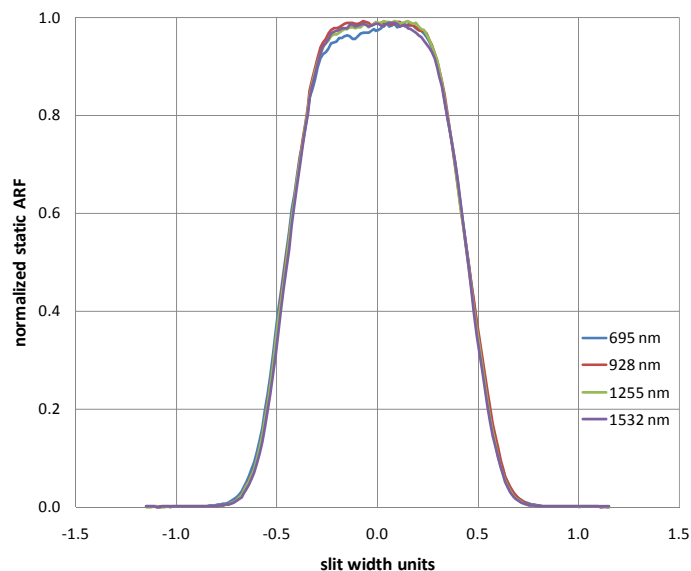


Figure 17. Measured along-track spatial response function for several wavelengths and the middle of the field.

7. CONCLUSIONS

We have constructed and tested a laboratory breadboard of a wide-field, high-throughput pushbroom imaging spectrometer, comprising a two-mirror telescope and a two-element spectrometer. Simple contact alignment methods for the telescope and spectrometer were implemented and met tolerances. A novel, bilinear groove, steeply concave diffraction grating was fabricated with grey scale X-ray lithography and exhibited high efficiency. The system demonstrated geometric uniformity of spectral and spatial response of better than 97%. The variation of spatial and spectral response function widths was at a similar level. With improvements in the detector and electronics uniformity and linearity, this spectrometer system can fulfill the requirements of demanding applications in Earth or planetary remote sensing.

ACKNOWLEDGMENTS

This research has been performed at the Jet Propulsion Laboratory, California Institute of Technology, under a contract with the National Aeronautics and Space Administration. We thank our science co-investigators in this project: Diana Blaney, Rob Green, and Glenn Sellar for discussions leading to the final configuration, and Sarath Gunapala for detector advice. We also thank Dan Wilson for discussions and hints on the grating and mask fabrication techniques, Eric Hochberg and Ron Holm for help with the system test setup, Larry Scherr and Len Wayne for help with detector characterization. Funding has been provided through NASA's Planetary Instrument Definition and Development

Program. Reference herein to any specific commercial product, process or service by trade name, trademark, manufacturer, or otherwise, does not constitute or imply its endorsement by the United States Government or the Jet Propulsion Laboratory, California Institute of Technology.

REFERENCES

- [1] Dyson, J., "Unit magnification optical system without Seidel aberrations," J. Opt. Soc. Am. 49, 713-716 (1959).
- [2] Mertz, L., "Concentric spectrographs," Appl. Opt. 16, 3122-3124 (1977).
- [3] Lobb, D. R., "Imaging spectrometers using concentric optics," Proc. SPIE 3118, 339-347 (1997).
- [4] Mouroulis, P., R. O. Green, and T. G. Chrien, "Design of pushbroom imaging spectrometers for optimum recovery of spectroscopic and spatial information," Appl. Opt. 39, 2210-2220 (2000).
- [5] Bezy, J-L., S. Delwart, G. Gourmelon, G. Baudin, R. Bessudo, and H. Sontag, "Medium-resolution imaging spectrometer (MERIS)," Proc. SPIE 2957, 31-42 (1997).
- [6] Warren, D. W., D. J. Gutierrez and E. R. Keim, "Dyson spectrometers for high performance infrared applications", Opt. Eng. 47 103601 (2008).
- [7] Johnson, W. R., S. J. Hook, P. Z. Mouroulis, D. W. Wilson, S. D. Gunapala, C. J. Hill, J. M. Mumolo, and B. T. Eng, "QWEST: Quantum Well Earth Science Testbed", Proc. SPIE 7086 708606-1, (2008).
- [8] Mouroulis, P., R. O. Green and D. W. Wilson, "Optical design for a coastal ocean imaging spectrometer", Opt. Express 16(12), 9087-9096 (2008).
- [9] Mouroulis, P., F. Hartley, D. Wilson, V. White, A. Shori, S. Nguyen, M. Zhang, and M. Feldman, "Blazed grating fabrication through gray-scale X-ray lithography", Opt. Express 11(3), 270-281 (2003).
- [10] Mouroulis, P., F. T. Hartley, R. E. Muller, D. W. Wilson, A. Shori, M. Feldman, L. Jiang, and T. R. Christenson, "Grating fabrication through X-ray lithography," Proc. SPIE 5173, 108-114 (2003).
- [11] Wilson, D. W., P. D. Maker, R. E. Muller, P. Mouroulis, and J. Backlund: "Recent advances in blazed grating fabrication by electron-beam lithography" Proc. SPIE 5173, 115-126 (2003).
- [12] Mouroulis, P., and M. McKerns: "Pushbroom imaging spectrometer with high spectroscopic data fidelity: experimental demonstration", Opt. Eng. 39, 808-816, (2000).
- [13] Green, R. O.: "Spectral calibration requirement for Earth-looking imaging spectrometers in the solar-reflected spectrum", Appl. Opt. 37, 683-690, (1998).